Engineering and Technology Journal e-ISSN: 2456-3358
Volume 09 Issue 12 December-2024, Page No.- 5569-5578
DOI: 10.47191/etj/v9i12.01, I.F. – 8.227

Optimization of Elaeis Guineensis Shell Ash Nanoparticles for Gas Turbine Blade Coating

Edeowede Abel Abhulimen[1], Thomas Ndyar Guma[2], Nnorom Achara[3]
[1,2,3] Mechanical Engineering Dept., Nigerian Defence Academy (NDA), Kaduna.

ABSTRACT: The nanoparticles of elaeis guineensis (oil palm) kernel shell ash was developed into recipe for the fabrication of composite coatings on gas turbine blades, with electrodeposition technique employed. To prepare the electrodeposition bath; 100g/l $ZnCl_2$, 5g/l Thiourea, 15g/l Boric acid, and 100g/l KCl were utilized and the recipe for the fabrication of the composite coatings were 0, 5, 10, 15, 20 and 25g/l of the nanoparticles. This paper tends to analyse the various percentage weight of the recipe making up the electrolyte, with a view to investigating and ascertaining the effectiveness of the coatings derived from each composition through; coating thickness, hardness value, surface roughness, X-ray Diffraction (XRD), electrical conductivity, tribology and microstructure analysis. Whereas the results of the investigation reveal that the performance of gas turbine blade was enhanced with the composite coatings, the 20g/l composition was found to be most effective. The decrease in the performance beyond this composition is attributable to the fact that the electrolyte became too viscous to promote easy flow of electrons during electrodeposition, as was similarly observed in previous work.

KEYWORDS: Optimization, Elaeis Guineensis, Nanoparticles, Gas Turbine, Coating

I. INTRODUCTION

The Palm Kernel Shell (PKS) is the hard part that enclosed the nut of palm kernel fruit and the shell parts obtained as residual waste after crushing and removal of nut in the palm oil mill during the extraction of kernel [1]. The palm kernel shell has estimated value of about 34.5% of a single ripe, fresh fruit [2] where in the year 2001 alone, the estimated value of 3.06 million metric tons was produced by Indonesia and Malaysia [3]. From this estimated value of 34.5% PKS from a single fruit, it could be established that the disposal of these biomass wastes will continue to pose major environmental problems.

The Gas Turbine (GT) is widely used in various industries to produce mechanical power and to drive various loads such as aircraft, trains, ships, electrical generators, pumps, gas compressors and tanks [4]. Its flexibility of operation makes it suitable for variable loads like compressor in transmission pipeline for oil and gas as well as marine propeller or road vehicles. The superiority of the gas turbine which makes it lucrative in today's world includes: a) its relatively fast startup time and hence, suitability for black start in the power industry; b) its relatively low installation as well as standby cost; c) its fewer auxiliaries, making the space required for its installation reasonably small; d) its tendency of being cited in varying locations and e) its relatively high Power to weight ratio etc. A turbine blade often referred to as "bucket", is the individual component which makes up the turbine section of a gas turbine and are responsible for extracting energy from the high temperature, high pressure gas produced by the combustor. The blades are often the limiting components of the gas turbine [5]. Blade platform contains the hot gas path and protects the rotor disc rim against inadmissible heating. The blade root consists of a fir-tree dovetail with two or three serrations which are inserted into mating grooves in the rotor discs and locked in the axial direction by means of keys, during installation. To survive in the difficult environment, turbine blades often use different methods of cooling in addition to being made of superalloys [6]. The need for better materials for the gas turbine blades has spurred much research in the field of alloys and manufacturing techniques, resulting in a long list of new materials and methods that make modern gas turbines possible [7]. Modern turbine blades often use nickel-based superalloys that incorporate chromium, cobalt, and rhenium [8], [9].

Advanced gas turbine engines operate at high temperatures in order to improve thermal efficiency and power output. In small gas turbines, the Turbine Inlet Temperature (TIT) could be about 870°C whereas in large modem machines, this figure is more likely around 1,400°C[10]. This operating temperature is far above the permissible metal temperature and often in excess of the melting point of Nickel based alloys (1200~1315°C). As the turbine inlet temperature increases, the heat transferred to the turbine blades also increases. To achieve reasonable durability goals, these thermal stresses must be limited otherwise complete melting of the blade could result, as evident in Plate 1. Such high temperature is often tolerated by special high temperature materials used for the Hot Gas Path of the GT and ceramic coatings, in addition to cooling arrangements built into the machine [11]. Bucket deterioration as a result of high operating

temperature include: cracks, dents, missing metals and corrosion [12]

Plate 1: Overheated 1st stage nozzle, up to complete melting.

Coating on the other hand refers to a covering applied to the surface of an object, usually the substrate for either a decorative purpose, functional purpose or both [13]. Coatings such as Paints and lacquers mostly serve dual purpose of protection and decoration on the substrate. Functional coatings may be applied to change the surface properties of a substrate, such as adhesion, wettability, corrosion resistance, or wear resistance [14].

A. Coating processes.

There is a wide range of coating processes employed to deposit varying types of material at thicknesses ranging from just a few microns, up to several millimetres. The different types of coatings can be categorized in many ways as given below in Figure 1**: Coating processes**.

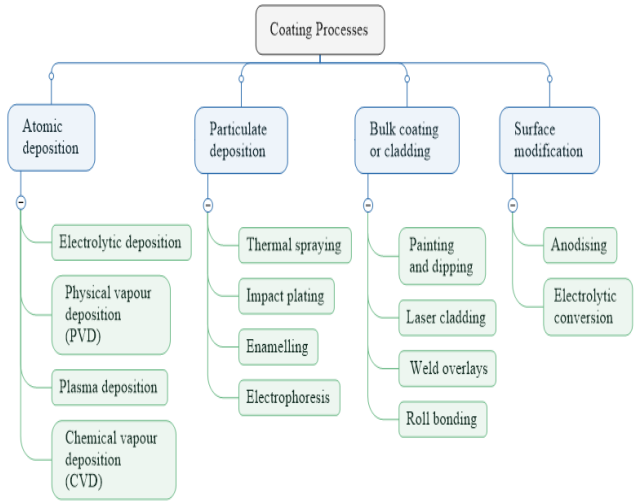

Figure 1: Coating processes

II. MATERIALS, EQUIPMENT AND EXPERIMENTAL PROCEDURE

This session entails; the materials, methods, equipment and procedure used in the preparation of the palm kernel shells into ash and further into nanoparticles, the processing of the coatings under this investigation, and also presents the details of the characterization tests and optimization which the coated samples were subjected to, in the course of this work.

A. Materials.

The palm kernel shells (PKS) as in Plate 2, were sourced from Ohordua, Edo State, Nigeria and the MS9001E Turbine Buckets (Plate 3) were sourced from Transcorp Power Plant in Ughelli, Delta State, Nigeria.

Plate 2: The palm kernel shells

Plate 3: Gas Turbine Buckets

B. Equipment

The equipment used in this research are; Metal mould, hydraulic press, Rockwell hardness, grinding and polishing machine, TEM (Jeol, JSM2010), ASAP 2020 Micromeritics surface area analyser, PANalytical X-PERT PRO diffractometer, Nanoparticle size analyser Model: HORIBA LB 550, Perkin Elmer spectrum 100 FT – IR spectrometer, pulverizing machine, Retsch Planetary Ball Mill PM 400, Scanning Electron Microscope (SEM), Erlenmeyer flask, mortar and pestle. Others are; 200keV electron beam, dropper, TGA Q50 thermogravimetric analyser, sample pan, TA Instruments' universal analysis 2000 software, aquarium pump, magnetic stirrer and rectifier.

C. Experimental procedure

1) ***Preparation of the Turbine blade samples:*** Before the coating process, the turbine blade was grounded and polished using metallographic grit sheets and alumina paste, and then soaked in 10% HCl solutions for 10mins, for proper cleaning. It was then washed with deionized water and dried. The prepared turbine blade was then cut into varying sample sizes as shown in Plate 4.

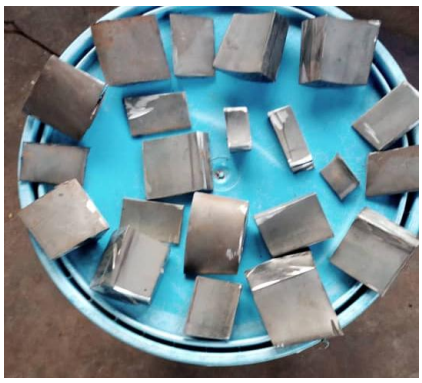

Plate 4: Prepared turbine blade samples

2) ***Production of the composite coating:*** The electrodeposition technique was used to develop the new composites. To prepare the electrodeposition bath, 100g/l $ZnCl_2$, 5g/l Thiourea, 15g/l Boric acid, and 100g/l KCl were utilized. The recipe for the fabrication of the composites coating were 0, 5, 10, 15, 20 and 25wt% PKSAnp. The chosen composition was made possible after preliminary experiment. With the aid of an aquarium pump and magnetic stirrer, the bath liquid was churned for 24hrs. The electrodes were wired with direct current from a rectifier and attached to the substrate, which served as the cathode and zinc metal, the anode, in a vertical position within the bath. A distance of 12mm from both side of the cathode and a current density of 2.5A/cm^2 was used in the electrodeposition. Plate5 shows the electrodeposition process whereas the coated samples are displayed in Plate 6.

Plate 5: The electrodeposition process

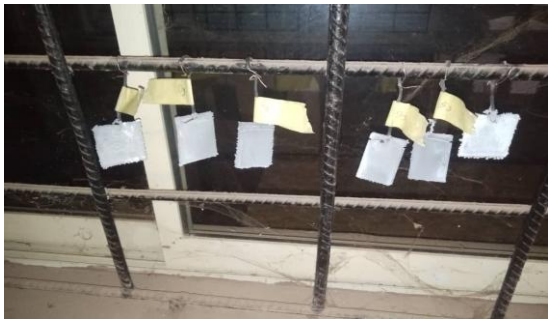

Plate 6: Samples after electrodeposition.

3) **SEM and EDS Analysis:** The microstructure of the coated samples was studied using a JOEL JSM 5900LV Scanning Electron Microscope, equipped with an Oxford INCA TM Energy Dispersive Spectroscopy (EDS) system, shown in Plate 7. The polished samples were firmly held on the sample holder using a double-sided carbon tape before putting them inside the sample chamber. The SEM was operated at an accelerating voltage of 5 to 20kV [15]. The signals derive from electron-sample interactions revealed information about the sample, including; external morphology (texture), chemical composition, crystalline structure and orientation of materials making up the sample. In this application, data were collected over a selected area of the surface of the sample and a 2-dimensional image was generated that displays spatial variations in these properties. Areas ranging from approximately 1cm to 5cm microns in width were imaged in a scanning mode using conventional SEM techniques (magnification ranging from 20X to approximately 30,000X, spatial resolution of 50 to 100nm). The Energy-Dispersive X-ray Spectroscopy (EDS) system which includes a sensitive x-ray detector, a liquid nitrogen dewar for cooling, and software for collecting and analysing energy spectra, focused the electron beam onto a region of the sample surface to perform elemental analysis of the test samples in an area scan mode. The detector was mounted in the sample chamber of the main instrument at the end of a long arm, which is itself cooled by liquid nitrogen.

Plate 7: The SEM Instrument with EDS detector [16]

4) ***Tribology***: The wear rate of the samples was measured using pin on disc machine by sliding it over a cast iron surface at a load of 20N, sliding speed of 5.02m/s and sliding distance of 500m. The initial weights of the samples were measured using a single pan electronic weighing machine with an accuracy of 0.0001g. During the test, the pin was pressed against the counterpart, rotating against a cast iron disc (hardness 65HRC) of counter surface roughness of 0.3µm by applying the load. A friction detecting arm connected to a strain gauge held and loaded the pin samples vertically into the rotating hardened cast iron disc, shown in Plate 8. After running through a fixed sliding distance, the samples were removed, cleaned with acetone, dried, and weighed to determine the weight loss due to wear. The difference in weight measured before and after tests, gives the wear of the samples.

Plate 8: Wear Resistance Test apparatus [17]

5) ***Hardness Value/Indentation Resistance:*** The Vickers hardness test method which is one of the most used hardness testing methods [18], was employed. The test procedure involves preparing, indenting, and then measuring the sample under a microscope to determine the diagonal lengths, and calculating the Vickers hardness number. It is a micro indentation test which was carried out with the help of filar microscope (standard 4X to 500X) and a deviation of the half diagonal for Vickers less than 5% (as shown in figure 2), for 10-15seconds, producing an indentation. With optical evaluation, the size of the indentation left on the surface of the test material by a pyramid-shaped diamond indenter (square base and interfacial angle of α = 136°) was measured under various loads, typically starting at 200gf. The test load was applied precisely and the Vickers hardness number was calculated (from Equation 1) by dividing the load by the surface area of the indentation, which was determined by measuring the lengths of the two diagonals created and taking the average.

$$HV = \frac{2P\sin\frac{136^0}{2}}{d^2} = \frac{1.854P}{d^2} \quad \text{.....Equation 1}$$

Where P = Load in kg, and d = Average length of opposite diagonals of impression in mm

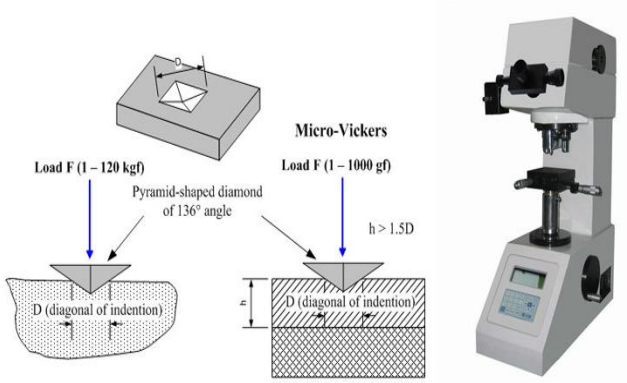

Figure 2 The Vickers hardness test [19]

6) ***Coating thickness:*** Plate 9 shows the Fischer COULOSCOPE CMS2 Coating Thickness Gauge with Coulometric DIN EN ISO 2177. It has a Measurement range of 0.5 – 50µm, controlled area size of; Ø3.2mm, Ø2.2mm, Ø1.5mm and Ø0.6mm; a graphic display size of 116 x 8mm, a memory of 3,000measurements and an ambient temperature range of 10 to 40^{0}C. The coated samples were cut along their widths, 20mm from the top, and the images taken at the middle of the coatings' cross sections. The preparation of the samples was done as per ASTM E1920 standard [20] while the thickness was evaluated at 10 equidistantly spaced points around an image, in accordance with ISO 1463 standard [21], in order to evaluate the average coating thickness at each taken image.

Plate 9: Fischer COULOSCOPE CMS2 Series Benchtop Coating Thickness Gauges [22].

7) ***Surface roughness:*** The surface roughness of the samples was measured using a non-contact stylus method with a Taylor Hobson roughness tester Surtronic 25 and a profilometer with Nobis chromatic confocal optical gauge using an optical aberration technique which focuses the white light at different profile heights (figure 3). Surface profile and the surface roughness parameters were determined: - Average Roughness (Ra), the arithmetic average variation from mean line over the evaluation length; - Maximum Height of the Profile (Rt), the distance from the highest peak to the deepest valley over the evaluation length; - Average Maximum Height of the Profile (Rz), the average Rt over five evaluation lengths and the surface finish was also studied using Samples of 3 x 3mm, detached from the surface and analyzed.

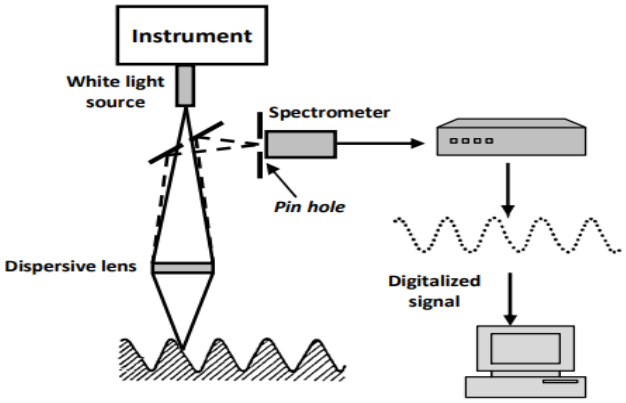

Figure 3: Non-contact optical surface roughness analysis [23]

8) ***Electrical Conductivity:*** A test apparatus was established to measure the electrical conductivity of the specimens. The schematic view of the established test apparatus is given in Figure 4. There were two Teflon parts mounted on

a rod and two copper parts mounted on the Teflon parts for the testing apparatus. One of the Teflon parts was fixed whereas the other was movable horizontally, so that the measurement length remained adjustable. The apparatus allowed the measurement of electrical conductivity of the specimens in longitudinal, transverse and thickness directions. In order to eliminate any inference of probe resistance, the measurements were performed with a four-probe-method [18]. First, the specimens were placed between the copper plates, and full contact was ensured by applying force, then the electrical conductivity of the specimens was measured with HM8118 LCR-Bridge. With three neat and doped specimens prepared for each direction, the measurements were repeated five times and the results were averaged. In order to further investigate the change of electrical conductivity with temperature in the thickness direction, the electrical conductivity of neat and carbon nanotube (CNT) doped materials were measured with Nova control Concept 50 Dielectric and Impedance Spectrometer at 1kHz frequency, between the temperatures −100˚C and 160˚C.

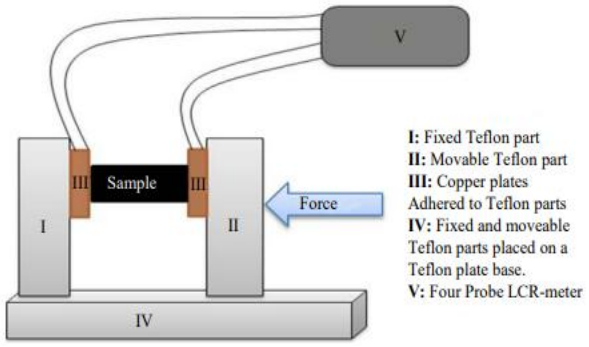

Figure 4: Electrical Conductivity setup, for the samples [24]

III. RESULTS AND DISCUSSION

A. Coating Thickness.

Figure 5 shows the coated samples' coating thickness. Under this investigation, we obtained a coating thickness of 88, 90.67, 97, 97.33, 103.67, 123, and 117.33 micrometers for; the substrate, 0, 5, 10, 15, 20, and 25g/l PKSAnp. The decrease in the coating thickness at 25g/l is attributable to the fact that the PKSAnp was too viscous at that concentration to ensure easy flow during electrodeposition, as was similarly observed in previous work [25].

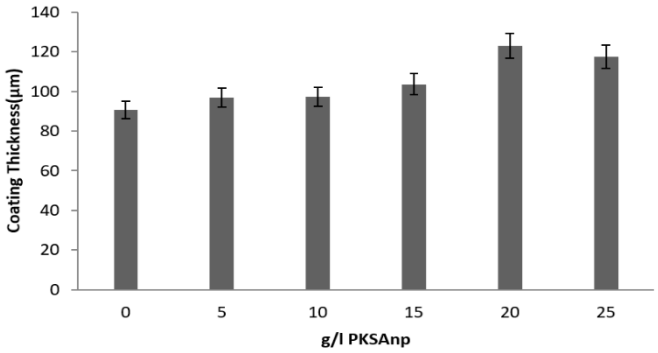

Figure 5: Variation of coating thickness with g/l of PKSAnp

B. Surface Roughness.

The findings of the surface roughness after the coating process, are shown in Figure 6. It is evident from the figure that the PKSAnp have a significant impact on the surface roughness; as the surface roughness values Zn-PKSAnp at 0, 5, 10, 15, 20, and 25g/l were found to be 0.41, 0.423, 0.473, 0.53, 0.552, and 0.563µm respectively. Additionally, it is evident that following coating, a hard and an uneven surface developed.

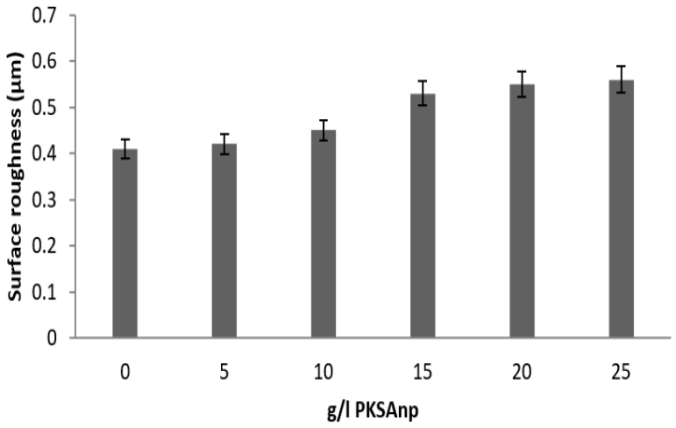

Figure 6: Variation of Surface roughness with g/l of PKSAnp

C. X-ray Diffraction (XRD) analysis.

Figure 7 displays the XRD pattern of the coated samples and the substrate. As shown in the figure, the substrate exhibited two prominent peaks, corresponding to α-Fe and Fe_3C at around 45 and 65 degrees, respectively. The similarity in the coated samples' XRD patterns was also seen in Figure 4.6. The evidence of ZnO was observed at 2θ =75° for the coated samples. However, only sample coated with 20g/l have a phase of SiO2 at 40.2° this is attributable to the fact that PKSAnp contains SiO_2. Since Zn was utilized as the coating's matrix material, the existence of ZnO in the Zn-coated samples may be explained, as having similarly been observed in previous research [26]. Moreover, the wide diffraction peak of the Zn-20g/l PKSAnp suggests that the crystalline behaviour of the Zn-PKSAnp system is greatly influenced by the presence of SiO_2 in the coating, thereby suggesting further that PKSAnp has been applied on the substrate's surface.

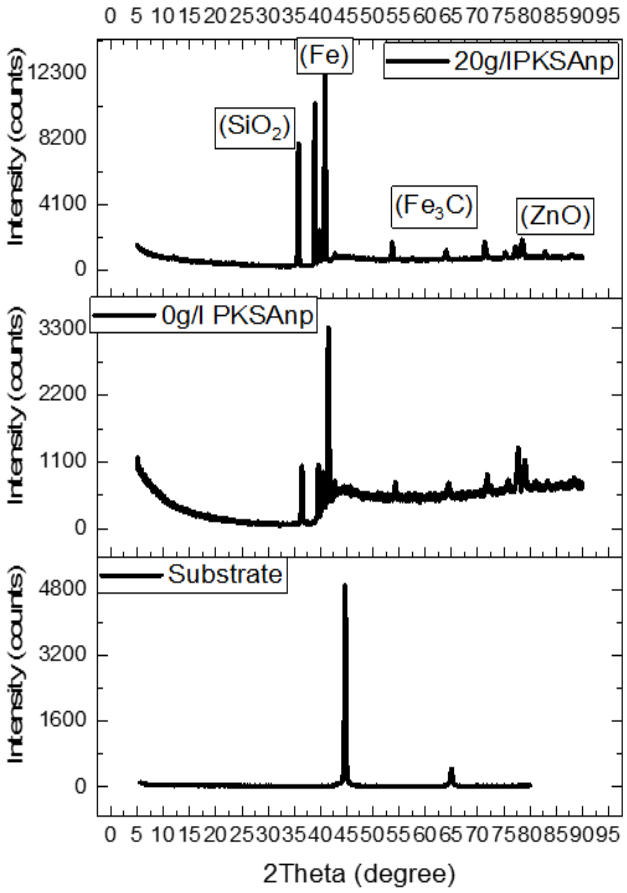

Figure 7: XRD pattern of the samples

D. ***Microstructure Analysis***.

The uncoated blade's microstructure is shown in Figure 8's SEM examination, with the lines created by the abrasive cutter visible due to surface scratches and no discernible organization. Figures 9-11 show the coated samples' SEM. The structural morphology of the substrate's SEM was found to vary from that of the coated samples -Figures 4.8-4.10. The microstructure alterations of the coated samples in comparison with the substrate (Figure 4.7) are equally visible. The surface of the uncoated sample seems translucent and free of material deposition; showing clearly, the presence of high-grain-size ferrite and pearlite. On the other hand, a thin, homogeneous coating of PKSAnp nanocrystalline nodules covers the whole surface of the coated sample. Increase in PKSAnp dissolution results in globules of Zn-PKSAnp, with Figure 4.10 showing a larger concentration of PKSAnp. Because of the enhanced PKSAnp dissolution, the SEM showed the strength of a second-phase bonding. The SEM equally reveals the coating effectiveness, devoid of any flaws such as cracks or holes. The uniformity of the coating can be attributed to; reduction of the nucleation density and grain refinement. This discovery is consistent with previous findings on microstructure and grain refinement [27], [28], [29] and that which shows that the use of oyster shell as a coating material produces a compact and dense deposit with few surface flaws and fewer crystallites [30], [31]. The EDS of the substrate shows a rise in the peaks of C and Fe and the lack of Si and Zn which indicates that carbon steel was employed. The presence of Zn and Si signals in Figures 4.8-4.10 is a strong indication that the coated samples were formed from PKSAnp materials.

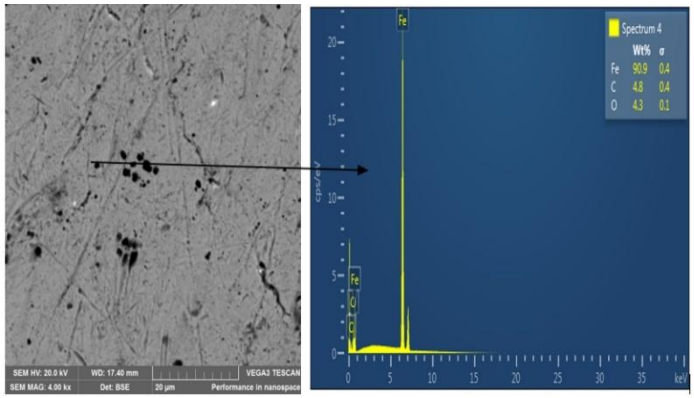

Figure 8: SEM/EDS pattern of the substrate

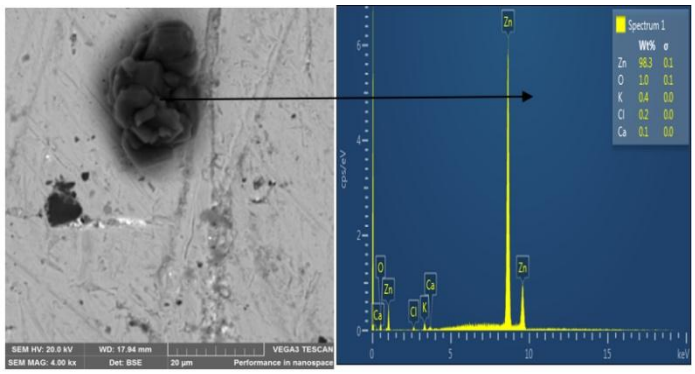

Figure 9: SEM/EDS pattern of the Zn-0g/l coating

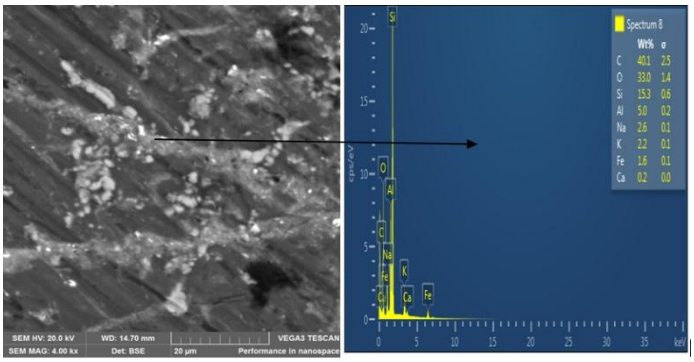

Figure 10: SEM/EDS pattern of the Zn-20g/l coating

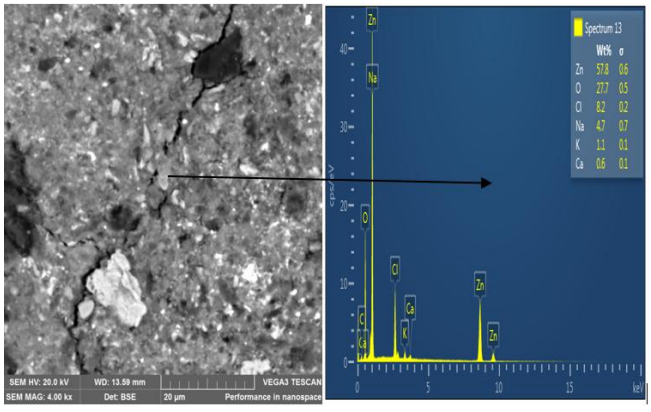

Figure 11: SEM/EDS pattern of the Zn-25g/l coating

E. ***Hardness value /Indentation Resistance Analysis***.

The results of the hardness values are shown in Figure 12. It was observed that the hardness values followed a similar pattern as the coating thickness described in section 4.5, having the hardness values increase in tandem with the coating thickness. This demonstrates that coating thickness and hardness levels are directly correlated. The hardness values of the 20g/l PKSAnp coated and substrate samples were found to be 395.34HV and 375HV respectively, indicating a 5.4% increase in hardness as a result of the coating. This increased hardness is attributable to the fact that the PKSAnp covered the substrate's surface thereby increasing the strain hardening, dispersive strengthening, grain refining, and dislocation density, which are known contributors to high hardness values [32].

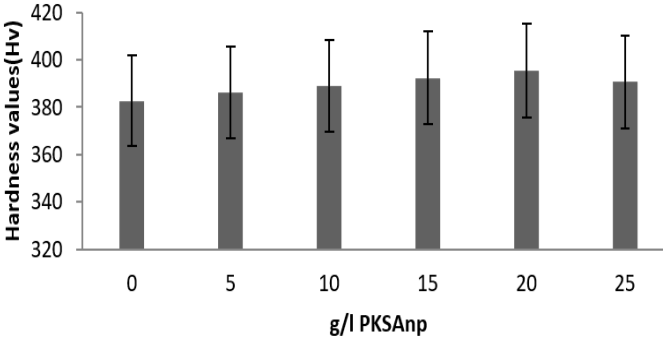

Figure 12: Hardness values of the samples

F. Electrical Conductivity Analysis.

The results of the electrical conductivity analysis are displayed in figures 13 to 18. Whereas the electrical conductivity pattern appears uniform, an indication that the samples possess similar electrical properties at the maximum frequency under review of about 300Hz, the electrical conductivity in Siemens per meter (S/m) was found to decrease with increase in the PKS concentration of the electrolyte from about 150,000S/m at 0g/l up to 100,000S/m at 20g/l. However, as the concentration increased to 25g/l, the electrical conductivity was found to increase, suggestive of a similar reason adduced to in section III (A) above. Lower electrical conductivity implies lower reaction rate and as such a reduction in the rate of sample's corrosion.

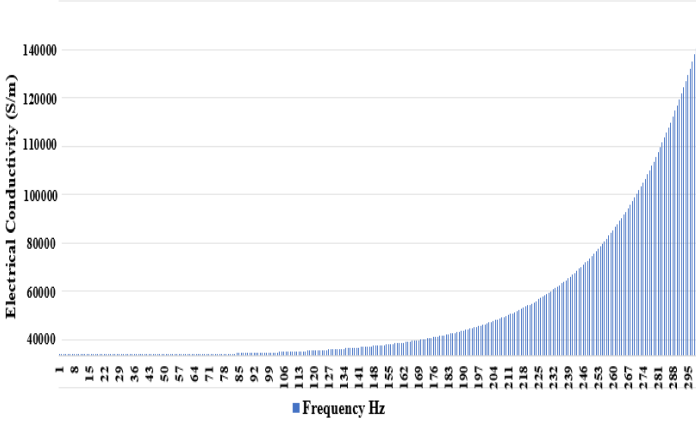

Figure 13: 0g/l PKS

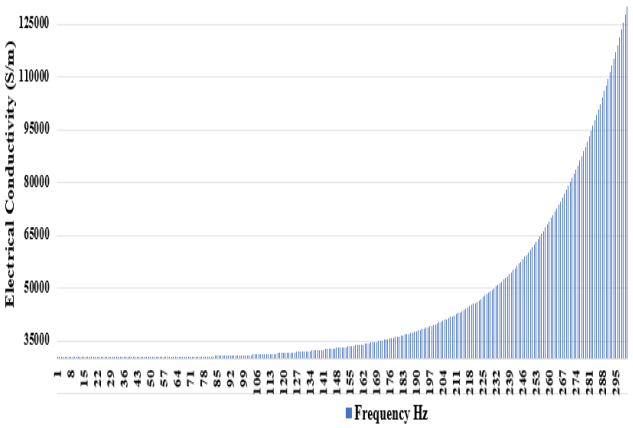

Figure 14: 5g/l PKS

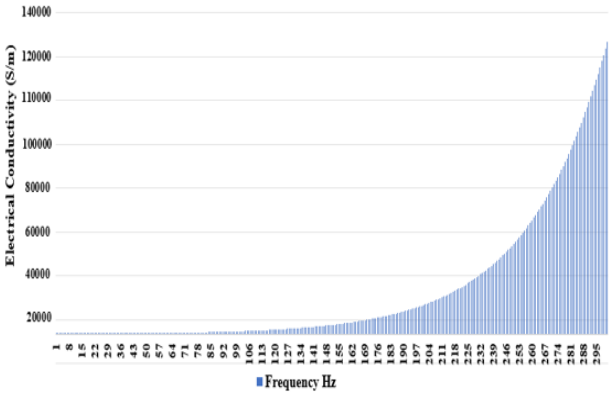

Figure 15:10g/l PKS

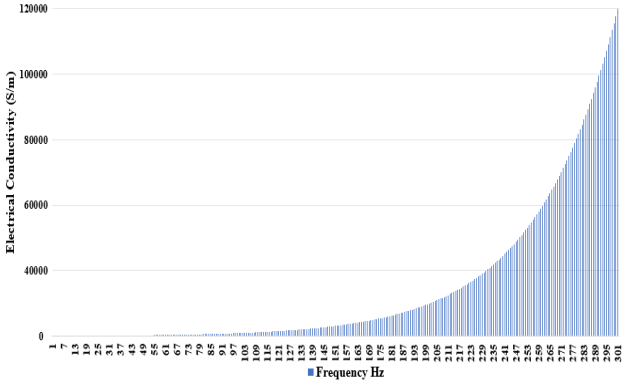

Figure 16:15g/l PKS

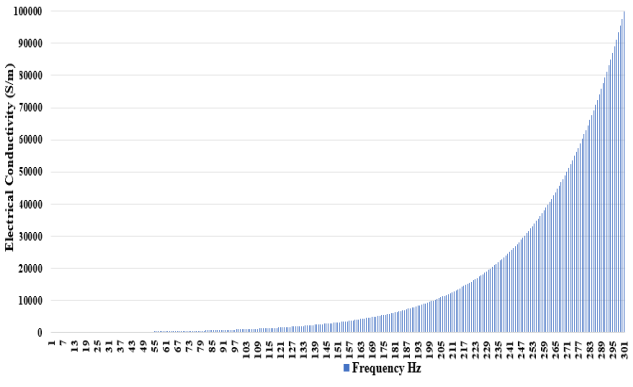

Figure 17: 20g/l PKS

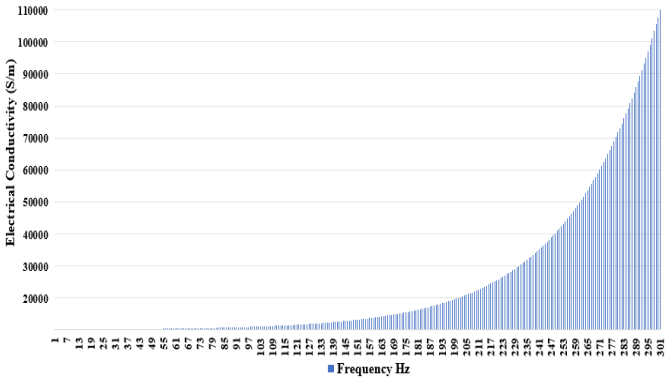

Figure 18: 25g/l PKS

G. *Tribology Analysis.*

The results shown in figures 19 to 23 indicate the samples performance regarding tribology in mm^3/Nm as well as in SEM images. With the coating, the wear rate of the samples was found to be very low, between $0.0005246mm^3/Nm$ and $0.02083mm^3/Nm$ for samples with 20g/l and 0g/l of PKS concentration of the electrolyte. This equally reveals that the optimum coating concentration was achieved at 20g/l PKS, being the lowest rate of wear amongst the tested samples.

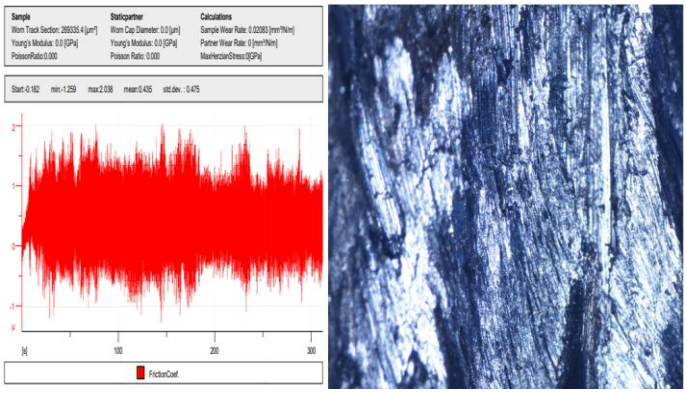

Figure 19: 0g/l PKS

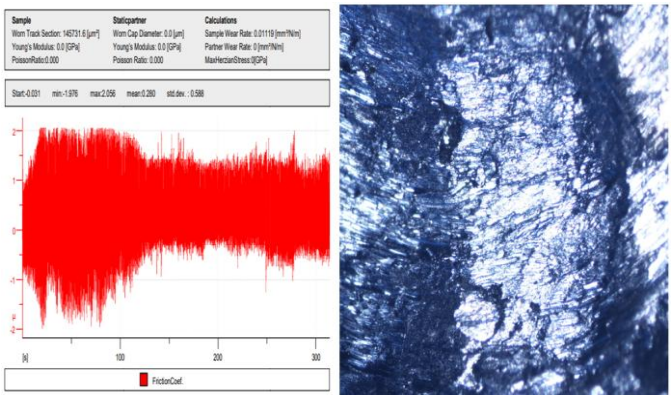

Figure 20: 5g/l PKS

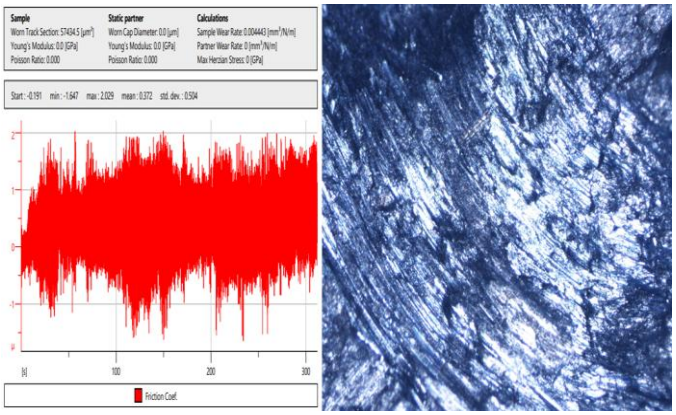

Figure 21: 10g/l PKS

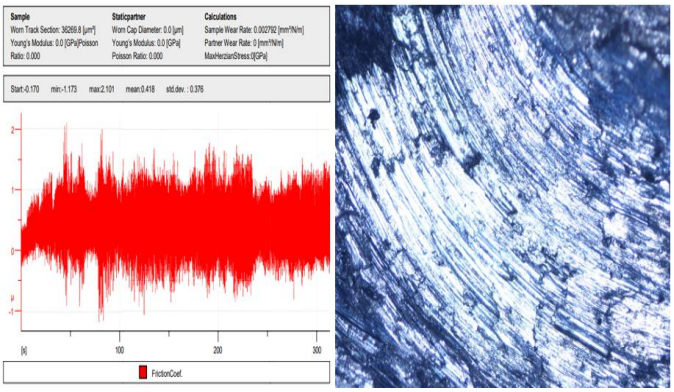

Figure 22: 15g/l PKS

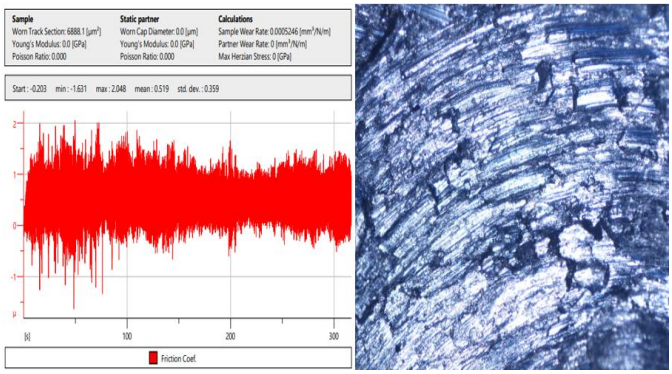

Figure 23: 20g/l PKS

IV. CONCLUSION

The effectiveness of nanoparticles of elaeis guineensis kernel shell ash in gas turbine blade coating has been established. The nanoparticles were developed into recipe for the fabrication of composite coatings on gas turbine blades, and electrodeposition technique was employed as the coating process. To prepare the electrodeposition bath, 100g/l $ZnCl_2$, 5g/l Thiourea, 15g/l Boric acid, and 100g/l KCl were utilized and the recipe for the fabrication of the composite coatings were 0, 5, 10, 15, 20 and 25g/l of the nanoparticles. Having thoroughly investigated and analysed each electrolyte composition for the coating samples through; coating thickness, hardness value, surface roughness, X-ray Diffraction (XRD), electrical conductivity, tribology and microstructure analysis, it is logical to conclude that the performance of gas turbine blade was enhanced with the

composite coatings, and that the 20g/l composition was found to be most effective and hence, optimal. The decrease in the performance beyond this composition is attributable to the fact that the electrolyte became too viscous to promote easy flow of electrons during electrodeposition, as was similarly observed in previous work.

REFERENCES

1. Abhulimen E. A., Guma T. N, and Achara N., (2024). Characterization of Palm Kernel Shell Ash Nanoparticles as Coating Material for High Temperature Applications. *International Journal of Latest Technology in Engineering Management & Applied Science*, vol. 13, no. 10, pp. 93–98. doi: 10.51583/IJLTEMAS.2024.131012.
2. Skawinska I. P. A., Jagustyn, B. (2013). "Evaluation of physicochemical properties of palm kernel shell as agro biomass used in the energy industry.," *CHEMIK*, vol. 67, pp. 552–559.
3. Oladosu, K.O., B. Kareem, B.O. Akinnuli and A.O. Alade, "Optimization of ash yield from the combustion of palm kernel shell and selected additives (Al2O3, CaO and MgO) using D-optimal design. Leonardo Electron.," *J. Pract. Technol*, vol. 15, pp. 9–18, 2016.
4. Saravanamutoo (2013). Gas Turbine Theory. Dorling Kindersley (India) Pvt. Ltd., licensees of Pearson Education in South Asia.
5. Boyce M. P. (2006). *Gas Turbine Engineering Handbook*, 3rd ed. Oxford: Elsevier. Pp118-134
6. Bogard D. G. and Thole K. A (2006). "Gas turbine film cooling," *J Propuls Power*, vol.22, no.2, pp.249–270. doi: 10.2514/1.18034.
7. Koff B. L. (2003). "Gas Turbine Technology Overview – A Designer's Perspective.," *AIAA/ICAS International Air and Space Symposium and Exposition*, vol. AIAA, no. Dayton, Ohio, pp.14–17.
8. Rhenium Statistics and Information. Accessed: Jun. 01, 2021. Available: https://www.usgs.gov/centers/nmic/rhenium-statistics-and-information.
9. GE Power Systems (1996). Cooling and Sealing air system, Tab 6. GEK106910. Pp. 1–6.
10. Abhulimen E. A. (2014). Cooling and Sealing air system, Favour Printers, pp. 21–27
11. L and K International Videotraining Program. Major Components, Ontario Canada L5A 4B4, no. 905
12. European Gas Turbines (1993). operation and maintenance guide- Hot Gas Path Inspection. 9E' 42 section 3. pp 2-12
13. Howarth G. A., and Manock H. L. (1997). Water-borne polyurethane dispersions and their use in functional coatings," Surf. Coatings Int., vol. 80, no. 7, pp. 324–328, doi: 10.1007/bf02692680
14. Coating. Retrieved from https://en.wikipedia.org/wiki/Coating. Accessed Sept.2021.
15. Ul-Hamid A., (2018). Components of the SEM, A Beginners' Guide to Scanning Electron Microscopy, pp. 15–76, doi: 10.1007/978-3-319-98482-7_2.
16. Kwon Y. E., Kim J. K., ju Y. Kim, J. G. and. Kim Y. J, (2019). Development of SEM and STEM-in-SEM grid holders for EDS analysis and their applications to apatite phases, *J Anal Sci Technol*, vol. 10, no. 1, doi: 10.1186/S40543-019-0186-0.
17. How to Test Wear Resistance of Ceramic Materials Accessed: Sep. 28, 2024. Available: https://www.preciseceramic.com/blog/how-to-test-wear-resistance-of-ceramic-materials.html.
18. Hardness test. Available: https://www.slideshare.net/slideshow/hardness-test-248540658/248540658. Accessed: Oct. 17, 2024.
19. Vickers hardness test - Google Search. Accessed: Oct. 17, 2024. Available: https://www.google.com/search?sca_esv=0162a739e8c9f12e&sxsrf=ADLYWIL5HjFwYad mlo4kl4wk8jiCqHUV0w.
20. E1920 Standard Guide for Metallographic Preparation of Thermal Sprayed Coatings. Accessed: Oct. 17, 2024. Available: https://www.astm.org/e1920-03r14.html.
21. Committee for Guides in Metrology, "First edition 2008. Evaluation of measurement data Supplement. Guide pour l'expression de l'incertitude de mesure'- Propagation de distributions par une méthode de Monte Carlo. Pp 223-276.
22. Fischer COULOSCOPE CMS2 Series Benchtop Coating Thickness Gauges. Available: https://old.pscontrol.ru/katalog/kontrol-pokrytiy-i-izolyacii/tolschinomery. Accessed: Oct. 17, 2024.
23. Surface Analysis of Machined Fiber Glass Composite Material." Accessed: Oct. 17, 2024.Available: ttps://www.researchgate.net/publication/267365450_Surface_Analysis
24. Akcin Y., Karakaya S., and Soykasap O. (2016). Electrical, Thermal and Mechanical Properties of CNT Treated Prepreg CFRP Composites," Materials Sciences and Applications, vol. 07, no. 09, pp. 465–483, doi: 10.4236/MSA.2016.79041.
25. Abbas K. H, Thear T., Abdul R., and Ali M. K., (2021). Evaluation of Hot Corrosion Properties for Nano-coated Superalloy, Journal of Applied Sciences and Nanotechnology, Vol.1, No.1
26. Vyavahare G. D., Gurav R. G., Jadhav P. P., Patil R. R., Aware C. B., and Jadhav J. P., (2018). Response surface methodology optimization for sorption of malachite green dye on sugarcane bagasse biochar and evaluating the residual dye for phyto and cytogenotoxicity. *Chemosphere*, vol. 194, pp.306–315. doi: 10.1016/j.chemosphere.2017.11.180.

27. Tedman-Jones S. N., McDonald S. D., Bermingham M. J., StJohn D. H., and Dargusch M. S., (2019). A new approach to nuclei identification and grain refinement in titanium alloys. *J Alloys Compd*, vol. 794, pp.268–284. doi: 10.1016/j.jallcom.2019.04.224.
28. Mendoza M. Y., (2017). Microstructures and Grain Refinement of Additive-Manufactured Ti-xW Alloys. *Metall Mater Trans A Phys Metall Mater Sci*, vol. 48, no.7, pp.3594–3605. doi: 10.1007/S11661-017-4117-7.
29. Zhang D., (2020). Grain Refinement of Alloys in Fusion-Based Additive Manufacturing Processes," *Metall Mater Trans A Phys Metall Mater Sci*, vol. 51, no. 9, pp.4341–4359. doi: 10.1007/S11661-020-05880-4.
30. Adams S. M., Anianwu F. O., and Aigbodion V. S., (2022). Ecofriendly new nanocomposites coating formulation of zinc reinforced with calcium oxide nanoparticles synthesis from oyster shell," *Journal of the Indian Chemical Society*, vol. 99, no.8. doi: 10.1016/j.jics.2022.100609.
31. Rosli S. A., (2024). Simple Thermal Treatment of Waste Oyster (Crassostrea belcheri) Shells for the Production of Calcium Minerals in Biomaterials Application, *Nano Biomed Eng.* doi: 10.26599/NBE.2024.9290074.
32. Aigbodion V. S. and Ezema I. C., (2020). Multifunctional A356 alloy/ PKSAnp composites: Microstructure and mechanical properties, *Defence Technology*, vol. 16, no.3, pp.731–736, doi: 10.1016/J.DT.2019.05.017.